Experimental Investigation of Primary and Secondary Features in High-Mach-Number Shock-Bubble Interaction

Devesh Ranjan, John Niederhaus, Bradley Motl, Mark Anderson, Jason Oakley, and Riccardo Bonazza*

Engineering Physics Department, University of Wisconsin-Madison, 1500 Engineering Drive, Madison, Wisconsin 53706, USA

(Received 7 September 2006; published 12 January 2007)

Experiments to study the compression and unstable evolution of an isolated soap-film bubble containing helium, subjected to a strong planar shock wave ($M = 2.95$) in ambient nitrogen, have been performed in a vertical shock tube of square internal cross section using planar laser diagnostics. The early phase of the interaction process is dominated by the formation of a primary vortex ring due to the baroclinic source of vorticity deposited during the shock-bubble interaction, and the mass transfer from the body of the bubble to the vortex ring. The late time (long after shock interaction) study reveals the presence of a secondary baroclinic source of vorticity at high Mach number which is responsible for the formation of counter-rotating secondary and tertiary vortex rings and the subsequent larger rate of elongation of the bubble.

DOI: 10.1103/PhysRevLett.98.024502 PACS numbers: 47.40.Nm, 47.20.Bp, 47.20.Ma

The Richtmyer-Meshkov instability (RMI) [1,2] is generated when a perturbed interface between two fluids is impulsively accelerated by a shock wave which is accompanied by the deposition of baroclinic vorticity on the interface due to the misalignment of local pressure and density gradients. The turbulent hydrodynamic mixing due to the RMI and the Rayleigh-Taylor instability (RTI) is of great importance to scientists and engineers in the fields of inertial confinement fusion (ICF) [3], astrophysics, and supersonic combustion. In the case of ICF, the RMI-RTI-induced turbulent mixing between the deuterium-tritium (DT) fuel and ablator material results in lowering the fusion yield, while in the case of a scramjet engine, it can improve the combustion process by enhancing the mixing of the air and the fuel (hydrogen) in the short burn time available.

The interaction of a shock wave with an isolated gas bubble of variable density is one of the simplest cases for studying the RMI/RTI induced mixing. Previous studies of the shock-bubble interaction include the seminal work of Haas and Sturtevant [4] and the more recent work of Layes *et al.* [5,6]. These previous experiments were conducted in horizontal shock tubes with the bubble supported by a holder and subjected to a $M < 1.3$ shock wave in air. The presence of a vortex ring structure was suggested by the shadowgraphs; however, due to the integral visualization technique employed, the detailed structure of the vortex was not captured. These experiments were later modeled numerically in two dimensions [7,8] with the results being in reasonable agreement with the experiment.

Experiments have been conducted at the University of Wisconsin shock-tube laboratory to obtain qualitative and quantitative data for the shock-bubble interaction at high Mach numbers, in an attempt to bridge the gap between very high Mach number laser driven experiments and low Mach number shock-tube experiments. Experimental results can be compared to the current theoretical models and numerical works studying shock accelerated inhomogeneous flows (AIF) [7–10]. The data can also be used for code validation and development of new theoretical models.

The experimental results from the interaction of a strong planar shock wave, $M = 2.95$, with an isolated helium bubble in nitrogen [heavy-light H/L case, Atwood number, $A = -0.76$] are presented in this Letter. The current study complements the previous work by Ranjan *et al.* [11] where the interaction of a strong planar shock wave $M = 2.88$ with an isolated argon bubble in nitrogen (L/H case) was studied. The experimental setup used here is a slightly modified version of the setup used previously. In the present experiments, the retractable injector has been inverted so that the bubble can rise freely once retracted from the injector, without hitting the injector itself. The bubble formation, retraction, and visualization technique (two shocked images per experiment) remain unaltered, and are outlined in Ranjan *et al.* [11]. Figure 1(b) shows the bubble at rest on the injector prior to the injector retraction, and Fig. 1(c) shows the free-rising bubble just before the shock wave arrival. Several experiments have been conducted and reproducibility of the initial condition between different experiments is quite good with bubble diameters

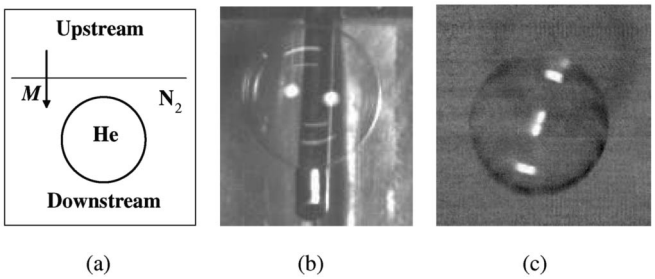

FIG. 1. Initial condition: (a) sketch of the bubble indicating the direction of propagation of the shock wave, (b) bubble at rest on the injector before the retraction, and (c) free-rising bubble just before the shock interaction.

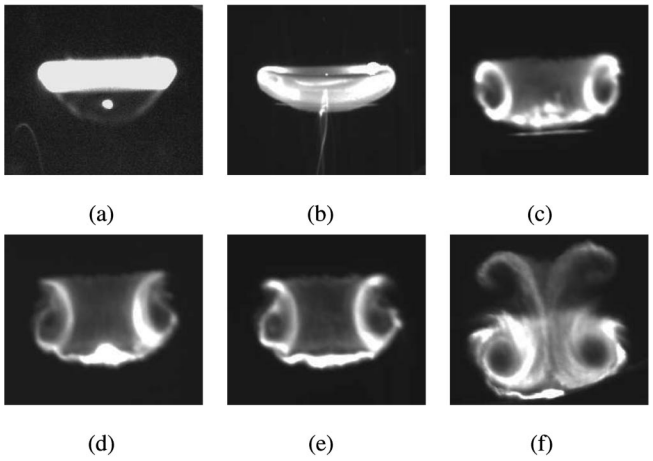

FIG. 2. Experimental images of a shocked ($M = 2.95$) helium bubble in N_2: (a) $\tau = 1.3$, (b) $\tau = 4.0$, (c) $\tau = 7.7$, (d) $\tau = 11.4$, (e) $\tau = 11.6$, and (f) $\tau = 23.8$. The time has been nondimensionalized as $\tau = t/\tau'$, where τ' is defined as $\tau' = D/(2 \times W_t)$.

in the range $D = 3.8 \pm 0.2$ cm and incident Mach numbers in the range 2.95 ± 0.04.

Figure 2 shows the evolution of the shocked spherical helium bubble after contact with a $M = 2.95$ shock wave with a velocity of 1040 m/s in N_2. The particle velocity behind the shock in N_2 is $u_p = 767$ m/s and the transmitted wave velocity in He is $W_t = 1971$ m/s (computed from 1D gas dynamics). The time has been nondimensionalized as $\tau = t/\tau'$, where τ' is defined as $\tau' = D/(2 \times W_t)$. The initial stage of the shock interaction with the bubble results in the compression of the bubble as seen in Fig. 2(a) where the transmitted shock wave is still inside the bubble. During this period of shock interaction, vorticity is deposited due to the misalignment between the pressure and density gradients which later leads to the formation of the primary vortex ring. Figure 2(b) shows the bubble after the shock wave has completely traversed it. It can be seen that the top portion of the bubble is caving inwards, on axis, due to the vorticity deposited during the interaction phase. Figure 2(b) shows a good qualitative comparison with the image (Fig. 1, frame 2) from the Layes *et al.* experiment [5] which was conducted at a low Mach number. This caving in is analogous to the phase reversal observed in single-mode H/L RMI experiments, and is a consequence of $\nabla\rho \times \nabla p$ vorticity deposition.

In Fig. 2(c) the formation of the primary vortex ring (hereafter referred to as the PVR) is observed. The white loops on the left and right of the image, with interior dark spots, are the cross section of the vortex ring at its midplane. The visualization technique highlights the fringes of the vortical cores but leaves the core itself as a distinct dark spot due to light-scattering soap-film particles being centrifuged outwards [12]. That is, the relatively dense soap-film particles are displaced from the vortex core by centrifugal forces that arise due to the large angular momentum of the vortex.

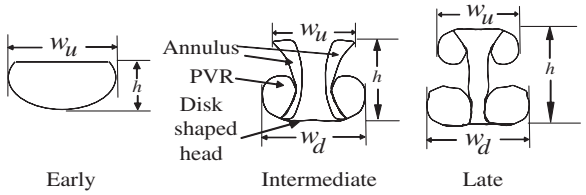

FIG. 3. Bubble length scales at different phases of evolution.

The next image in time, Fig. 2(d), has three notable features, which are labeled in the schematic diagram in Fig. 3. The first feature is the PVR clearly distinguished by its dark core in Fig. 2(d). An axial velocity in the flow field induced by the PVR appears to entrain fluid from the center portion of the bubble, swirling it into the vortex ring. The second feature is the disk-shaped head of the bottom of the bubble, which appears as a bright lateral swath in the 2D image connecting the left and right loops. The third feature is the annulus (it appears as bright arc in the 2D image) connected to the vortex ring and top of the bubble. The orientation of this arcing filament indicates the motion of helium being swept from the bubble interior into the PVR. Further, its orientation is indicative of the PVR's sense of rotation: clockwise on the left and anticlockwise on the right. This sense of rotation corresponds to the sign of the $\nabla\rho \times \nabla p$ term in the vorticity equation [4,13]. Figures 2(d) and 2(e) show good agreement with each other for images obtained from two different experiments. The motion of fluid drawn into the PVR implied from Figs. 2(d) and 2(e) accounts for the increased size of the PVR seen in Fig. 2(f) which is characterized quantitatively below.

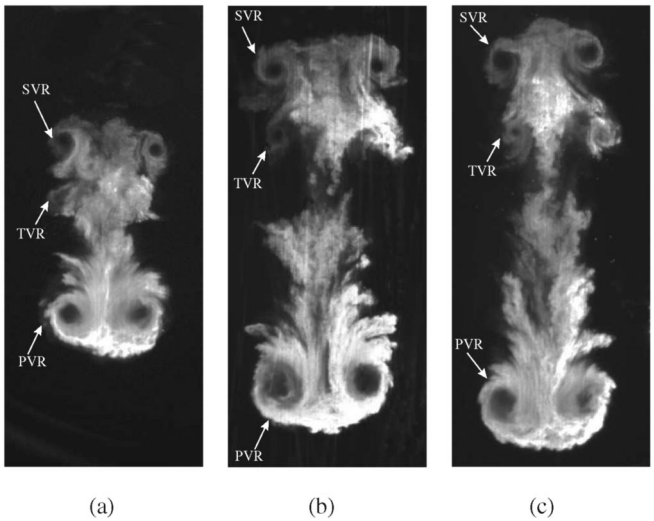

FIG. 4. Experimental images of a shocked ($M = 2.95$) helium bubble in N_2 showing secondary and tertiary vortex rings: (a) $\tau = 46.3$, (b) $\tau = 63.5$, and (c) $\tau = 69.5$. The time has been nondimensionalized as $\tau = t/\tau'$, where τ' is defined as $\tau' = D/(2 \times W_t)$.

TABLE I. Circulation results: experimental values for the primary (Γ_{PVR}) and secondary (Γ_{SVR}) vortex ring, and model values (Γ_{PB}, Γ_{YKZ}).

τ	M	u_p [m/s]	D [cm]	Γ_{PVR} [m^2/s]	Γ_{SVR} [m^2/s]	Γ_{net} [m^2/s]	Γ_{PB} [m^2/s]	Γ_{YKZ} [m^2/s]
23.8	2.95	768	3.81	20.9	−5.2	15.7	35.9	11.5
25.4	2.94	765	3.25	14.9	−3.1	11.8	30.6	9.8

Figure 4 shows the presence of secondary and tertiary counterrotating vortex rings in the flow field, which are absent in the case of low Mach number experiments [4,5]. These features are generated by complex shock refraction and reflection phenomena arising at high Mach numbers which are visible in simulations reported by Levy *et al.* [14]. A very small portion of helium appears to be stripped off from the top part of the PVR, which is entrained by the secondary vortex ring (SVR). In Fig. 4(a) some fine-scale turbulent structures can be seen on the bottom of the PVR.

In Fig. 4(b) and 4(c) one can clearly identify the three distinct vortex rings: the PVR at the bottom of the image, the SVR at the top of the image, and a tertiary vortex ring (TVR) just below the SVR. The SVR and TVR have the same sense of rotation (opposite to the PVR) due to which the region between them has an alternating vorticity field associated with a stagnation-type flow field. It can be surmised from these images that the strongest vorticity field is associated with the PVR. Most of the fluid (ambient N_2) in the region between the TVR and PVR is being pulled towards the PVR. This is observed from the long tails, or dendritelike structures, associated with the PVR, visible in Fig. 4(b). One can also observe that the core of the PVR becomes distorted and no longer has a circular cross section. Finally, in Fig. 4(b) and 4(c), the pinching off of the SVR and TVR from the PVR can be seen.

The observed separation of the SVR and TVR from the PVR is borne out in the measured velocities of the vortex rings. Figure 5 shows the measured vortex ring velocity, V_v, nondimensionalized by the shocked gas (N_2) particle speed u_p as a function of time. The downstream ring velocity (PVR) is higher than that of the flow. It shows good agreement with the predicted values from the Picone and Boris velocity defect model [7] and the previous trend shown for low Mach number helium experiments [5]. It is also consistent with the trend seen in the Haas and Sturtevant experiments [4], where the velocity V_v/u_p was observed to decrease substantially with an increase in shock strength. The upstream ring (SVR) moves more slowly than the flow. This is due to the SVR having an opposite sense of rotation than the PVR.

Circulation for the PVR and the SVR is calculated using Kelvin's model [4] formulated for a moving vortex ring. Table I shows the comparison between the circulation calculated from the experimental images and values predicted by different models [7,10]. It is observed that the

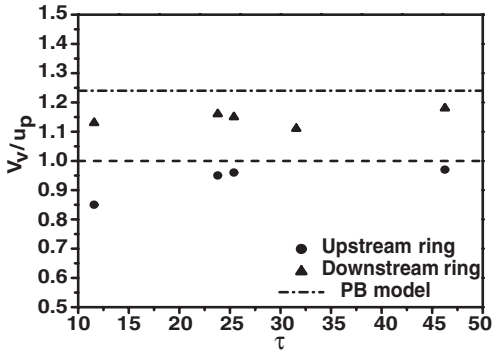

FIG. 5. Vortex ring velocity as a function of time.

Picone and Boris model (PB) overpredicts the net circulation by as much as a factor of 2 while the Yang, Kubota, and Zukoski model (YKZ) slightly underpredicts the circulation. It can also be seen that the majority of the vorticity is associated with the PVR.

Figure 3 is a drawing of the relevant length scales of the shocked bubble at different phases of evolution. The quantitative measurements include the overall height h, the maximum upstream width w_u, and the maximum downstream width w_d. In the analysis, the length scales are

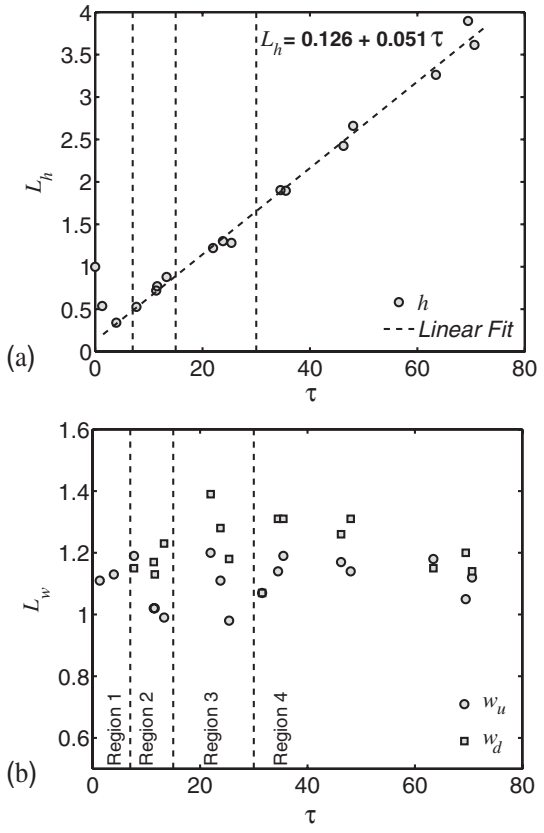

FIG. 6. Length scales w_u, w_d, and h (see Fig. 3) normalized by initial bubble diameter D, plotted as a function of the dimensionless time τ.

nondimensionalized by the initial bubble diameter, e.g., $L_h = h/D$. Figure 6 shows the evolution of the axial (height) and lateral (width) extents of the bubble. Four regions of interest have been labeled on the width plot separated by vertical dashed lines to facilitate the description of the evolution. The earliest post-shock images show an initial flattening of the bubble caused by compression due to shock interaction. The height plot in Fig. 6(a) shows compression taking place until $\tau = 4.0$. The initial flattening can be observed in region 1 of the width plot [Fig. 6(b)] where L_{w_u} reaches a local maximum. Region 1 is denoted as this early phase of evolution up to $\tau = 7.0$.

In the next phase of the bubble evolution [see Fig. 6(b)], region 2, L_{w_u} starts decreasing with an increase in L_{w_d}. This can be interpreted as a mass transfer process with fluid being drawn into the PVR from the body of the bubble as noted in the discussion of Fig. 2. These changes in the relative sizes of the upstream and downstream features are also evident in the experimental images of Haas and Sturtevant [4] and Layes *et al.* [5], for a shocked spherical helium bubble at $M < 1.3$. This interpretation views the behavior of the bubble as incompressible at this stage. Such an interpretation is justified by the simulations of Giordano and Burtschell [8] at low Mach numbers which suggest that the bulk density of the bubble changes very little at this time. It is further justified by the observation that the bubble is free of shocks and rarefactions at this stage.

The height grows linearly after the compression phase, and the rate of axial elongation ($\alpha = dL_h/d\tau$) of the bubble is measured to be $\alpha = 0.051$. Layes *et al.* reported $\alpha = 40.8$ m/s (Table I, [6]) for low M experiments, which in the nondimensional form is $\alpha = 0.024$. The observed rate of elongation in the present study is twice the value reported by Layes *et al.* [6], and the difference is attributed to the formation of the secondary vortex ring (counter-rotating) which is a consequence of the higher shock strength. Following region 2, a sudden decrease is observed in L_w, due to the shock wave reflected from the shock-tube side walls which originated when the incident shock wave was refracted off the surface of the bubble (this can be attributed to the presence of the soap film). Finally, in region 4, L_w reaches a plateau at late times.

The results presented in this Letter describe the development of a helium bubble accelerated by a shock wave $M = 2.95$. The planar laser imaging technique helps to characterize the vortex rings formed following the shock wave-bubble interaction much more distinctly than in previous work. From the width data it is concluded that there is mass transfer from the body of the bubble to the PVR. For the first time, the evidence of a secondary baroclinic source of vorticity associated with features introduced at high M is revealed, which leads to the formation of the SVR and TVR which separate from the PVR over time. At late time, the bubble velocities reach a constant value which is in good agreement with previous work, and the circulation measurement shows a reasonable agreement with the YKZ model. The rate of axial elongation of the bubble is found to be $\alpha = 0.051$, which can be used as quantitative value for comparison with simulation.

This research was sponsored by the National Nuclear Security Administration under the Stewardship Science Academic Alliances program through DOE Research Grant No. DE-FG52-03NA00061.

*Email address: bonazza@engr.wisc.edu
Electronic address: http://silver.neep.wisc.edu/~shock/

[1] R. D. Richtmyer, Commun. Pure Appl. Math. **13**, 297 (1960).
[2] Y. Y. Meshkov, NASA Tech. Transl. **F-13**, 074 (1970).
[3] J. D. Kilkenny, Phys. Plasmas **1**, 1379 (1994).
[4] J.-F. Haas and B. Sturtevant, J. Fluid Mech. **181**, 41 (1987).
[5] G. Layes, G. Jourdan, and L. Houas, Phys. Rev. Lett. **91**, 174502 (2003).
[6] G. Layes, G. Jourdan, and L. Houas, Phys. Fluids **17**, 028103 (2005).
[7] J. M. Picone and J. P. Boris, J. Fluid Mech. **189**, 23 (1988).
[8] J. Giordano and Y. Burtschell, Phys. Fluids **18**, 036102 (2006).
[9] N. J. Zabusky, Annu. Rev. Fluid Mech. **31**, 495 (1999).
[10] J. Yang, T. Kubota, and E. E. Zukoski, J. Fluid Mech. **258**, 217 (1994).
[11] D. Ranjan, M. Anderson, J. Oakley, and R. Bonazza, Phys. Rev. Lett. **94**, 184507 (2005).
[12] W. Merzkirch, *Flow Visualization* (Academic, New York, 1987), 2nd ed.
[13] J. W. Jacobs, Phys. Fluids A **5**, 2239 (1993).
[14] K. Levy, O. Sadot, A. Rikanati, D. Kartoon, Y. Srebro, A. Yosef-Hai, G. Ben-Dor, and D. Shvarts, Laser Part. Beams **21**, 335 (2003).